BNL-225116-2023-JAAM

GRP-COEE-26

Oxygen redox chemistry: A new approach to high energy density world

X. Cai, E. Hu

To be published in "Next Materials"

December 2023

Chemistry Department

Brookhaven National Laboratory

U.S. Department of Energy

USDOE Office of Energy Efficiency and Renewable Energy (EERE), Office of Sustainable Transportation. Vehicle Technologies Office (VTO)

DISCLAIMER

Oxygen redox chemistry: a new approach to high energy density world

Xinyin Cai[a], Zulipiya Shadike[a*], Nan Wang[b], Lin Liu[a], Enyuan Hu[b*], Junliang Zhang[a*]

[a]Institute of Fuel Cells, School of Mechanical Engineering, Shanghai Jiao Tong University, Shanghai 200240, China
[b]Chemistry Division, Brookhaven National Laboratory, Upton, NY 11973, USA

*Email: zshadike@sjtu.edu.cn; enhu@bnl.gov; junliang.zhang@sjtu.edu.cn

Abstract

Sodium-ion batteries (SIBs) have been considered as promising candidates for large scale energy storage systems due to the great abundance of sodium resources. For sodium layered transition metal oxide cathode materials, oxygen redox can increase the energy density by enabling extra capacity and delivering high voltage. Here we provide a comprehensive overview of oxygen redox in SIBs from the perspectives of mechanism, challenges, and solutions. The previous studies on voltage hysteresis, capacity decay and oxygen release induced by oxygen redox as well as the effectiveness of different strategies including superlattice engineering, elemental substitution, and surface modification on the electrochemical performances of cathode materials with oxygen redox are comprehensively summarized with typical examples. Finally, the remaining challenges and the future research direction are discussed.

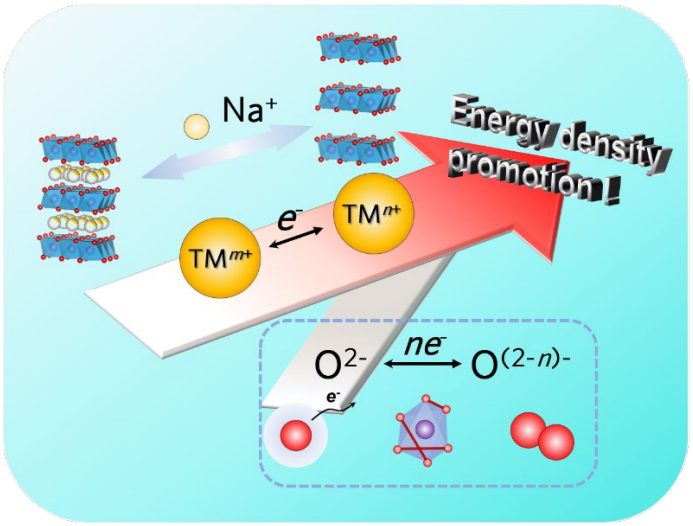

Table of content the oxygen redox largely promotes the energy density of the SIBs cathode through extra capacity and high potential provided by oxygen redox (oxygen electron holes, O—O dimers, O_2 molecules)

1. Introduction

The development of electrical energy storage with high energy density is of great significance to integrate renewable energy sources and realize carbon neutralization [1-3]. With the relatively high energy density and long cycle life, rechargeable lithium-ion batteries (LIBs) have become the technology of choice for electrical energy storage [4-6]. Since lithium-ion batteries were invented in the 1990s, they have been widely utilized in portable electronic devices and electric vehicles [7-9].

Compared with lithium, sodium has much more abundance in the Earth's crust and lower cost. Therefore, sodium-ion batteries (SIB) have been considered as promising candidates for large-scale energy storage with significant advantages over LIB [10-14]. To achieve high energy density SIBs, a great number of efforts have been made to develop high performance electrode materials in the past few years [15]. According to the price assessment, cathodes are critical to the SIBs because the cost proportion of cathodes is as high as 32.4% [16, 17]. Thus, it is very important for SIBs to develop cathode materials with high energy density and low cost.

As one of the categories of the cathode materials, sodium layered transition metal oxides (Na_xTMO_2, TM = transition metal) have been attracted much attention due to

their low cost (especially Mn-based cathodes), high capacity and tunable compositions [18]. Layered transition metal oxide cathodes of SIBs can be classified into two main categories, P2-type and O3-type, in which "P" and "O" refer to the different environments for Na^+ sites between TMO_2 layers: "P" corresponds to the prismatic site while the "O" corresponds to the octahedral site. The number after the "O" or "P" signifies the number of TMO_2 slabs that are describing the cell; In P2-type oxides, Na-ion coordination with oxygen exhibits a prismatic stacking. The oxygen arrangements can be described as "ABBA…". In O3-type oxides, there is the octahedral stacking between Na and O, where the oxygen atoms arrange as "ABCABC…. Typically, the energy density of electrode material is determined by the working potential and specific capacity. Meanwhile, the energy density can be increased by promoting more redox reaction or increasing redox potential of cathode materials [19]. For the traditional layered oxide cathodes, the capacity is mainly provided by the redox of transition metal elements with variable valences. Interestingly, in certain layered oxides such as $Li_{1.2}Ni_{0.13}Co_{0.13}Mn_{0.54}O_2$, $Li[Li_{0.2}Ni_{0.2}Mn_{0.6}]O_2$, Li_2IrO_3, the oxygen has been discovered to be able to participate in the charge compensation during charging and discharging [20-22]. More importantly, the oxygen possesses a higher redox potential than most of transition metals, resulting in higher energy density of the cathode materials [23]. However, irreversible oxygen redox reaction induces irreversible phase transitions, oxygen loss during charging, structure degradation as well as capacity loss [24-27]. Therefore, it is essential to discover cathode material with more reversible oxygen redox chemistry to further promote the energy density of SIBs. During the past few years, a great number of researches have been carried out to explore the nature of oxygen redox chemistry, including the charge compensation mechanism, local structure evolution, performance optimization and so on [28-31]. Here we provide an overview of oxygen redox in SIBs to better understand its advantages and challenges in layered transition metal oxides and to provide suggestions for designing SIBs cathodes with high energy density.

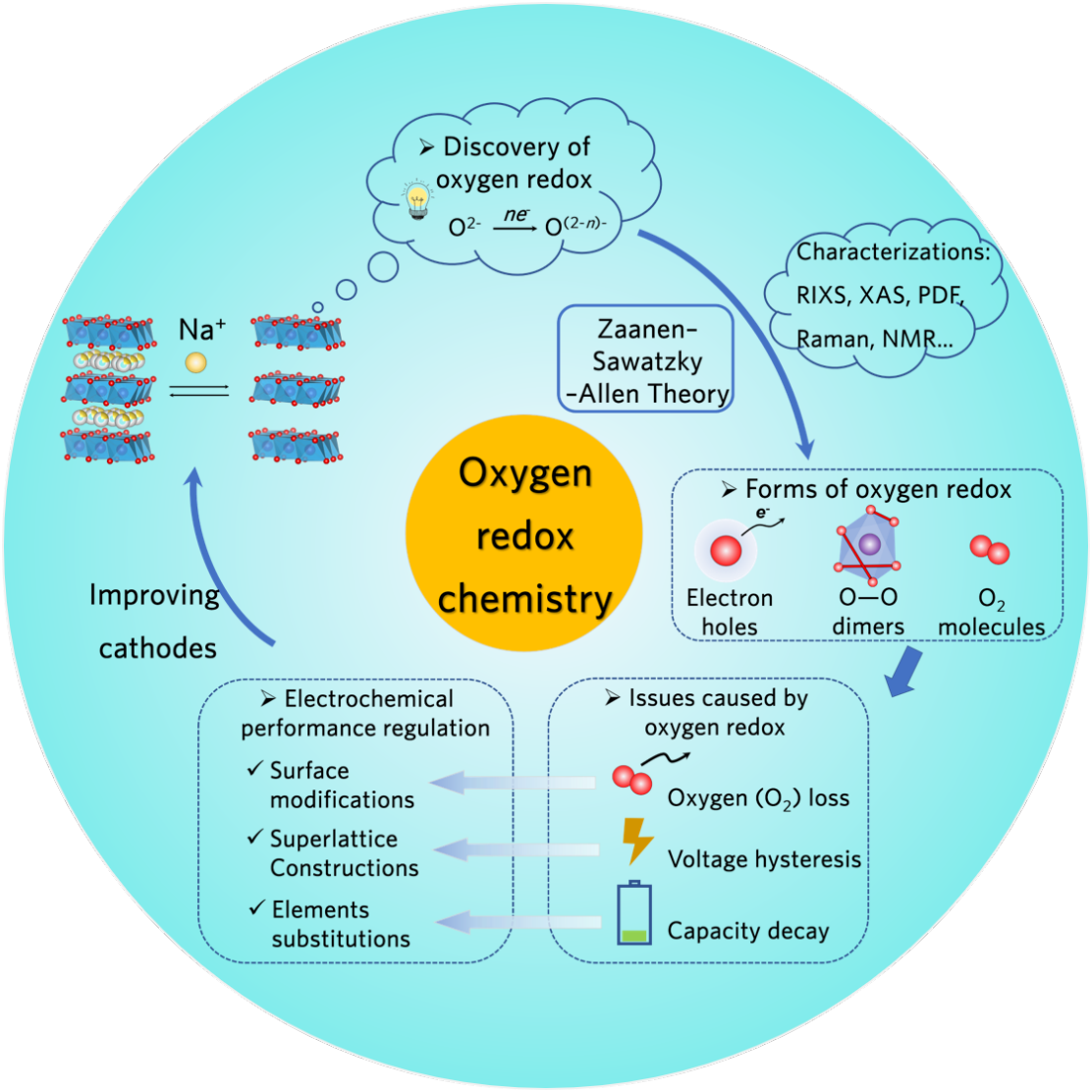

Figure 1 | Schematic map of research route of illustrating oxygen redox chemistry.

This review provides timely update of the recent progress of SIB cathodes with typical oxygen redox chemistry to address several scientific points as shown in **Figure1**: i) What is the nature of oxygen redox processes? ii) How to realize reversible oxygen redox through material design? iii) What is the key challenge of SIBs cathode with oxygen redox chemistry and how to overcome it? Firstly, the discovery of oxygen redox chemistry and relevant theory have been discussed with detailed examples. Three types of well-known processes of oxygen redox and relevant characterization techniques for probing charge compensation mechanism have also been described. Subsequently, typical issues caused by oxygen redox and the corresponding strategies to promote a reversible oxygen redox process are discussed. Finally, we performed a summary of the

latest findings and proposed the possible directions to develop SIBs cathodes with oxygen redox chemistry in the future. This review provides critical guidance for better understanding the oxygen redox chemistry in layered transition metal oxides for SIBs.

2. Discovery of oxygen redox chemistry

In early 2013, Yamada's group and collaborators reported the electrochemical properties of a novel layered Na_2RuO_3 [32] and proposed its special charge compensation mechanism with oxygen redox reaction [33]. They compared electrochemical behavior of Na_2RuO_3 (disordered Na_2RuO_3) with honeycomb ordering Na_2RuO_3 (ordered Na_2RuO_3) and demonstrated that ordered Na_2RuO_3 delivers higher capacity. By investigating the structural evolutions, the sodium storage mechanisms of disordered Na_2RuO_3 and ordered Na_2RuO_3 were proposed as shown in **Figure 2**a. With the Na^+ extraction from Na_2RuO_3 in charging process, the ordered $[\square_{1/3}Ru_{2/3}]O_2$ slabs in ordered Na_1RuO_3 can accommodate the RuO_6 octahedra distortion by shrinking the O—O distance to 2.580(4) Å. Such a decreased bond distance promotes the energy level of the antibonding σ^* orbital of the O—O, which facilitates oxygen redox reaction. However, the RuO_6 octahedra distortion cannot be accommodated in disordered Na_1RuO_3 that consists of disordered $[Na_{1/3}Ru_{2/3}]O_2$ slabs because of the long length of O—O distance and the energy level of antibonding O—O σ^* orbital being below the Fermi level. Thus, they regarded honeycomb ordering as the key to oxygen redox reaction. Moreover, similar to Na_2RuO_3, other lithium rich layered cathodes with alkali metal (AM) ions in transition metal layer exhibited obvious oxygen redox reaction [34]. The excess AM ions in compounds can form "AM^+—O—AM^+" configurations, in which the O 2*p* orbitals overlap with the 2*s* orbitals of AM^+ cations. Ceder *et al.* proposed that the ionic nature of the special configurations induced O non-bonding 2*p* states at the top of O-valance band and this has been regarded as the origin of oxygen redox [35]. Komaba *et al.* developed P2-type $Na_{2/3}[Mg_{0.28}Mn_{0.72}]O_2$ cathode and observed very similar "oxygen redox phenomenon" with anomalously large capacity of >200 mAh g^{-1}. However, no clear evidence for oxygen redox was shown [36]. In

2018, Bruce's research group and collaborators utilized resonant inelastic X-ray scattering (RIXS) to demonstrate that oxygen redox chemistry can also be triggered without having alkali-metal ions in the transition metal layer as in the case of $Na_{2/3}[Mg_{0.28}Mn_{0.72}]O_2$ [37]. In Na-deficient O2-type $Na_0[Mg_{0.28}Mn_{0.72}]O_2$ structure, O 2*p* orbitals interact with one Mg^{2+} and two Mn^{4+}. In this local structure, Mg 3*s* states exhibit higher energy than O 2*p* and the formation of weak ionic Mg—O bonds elevate the energy of O 2*p* states, which places the O 2*p* orbitals close to the Fermi level and promotes oxygen redox chemistry in P2-type $Na_{2/3}[Mg_{0.28}Mn_{0.72}]O_2$.

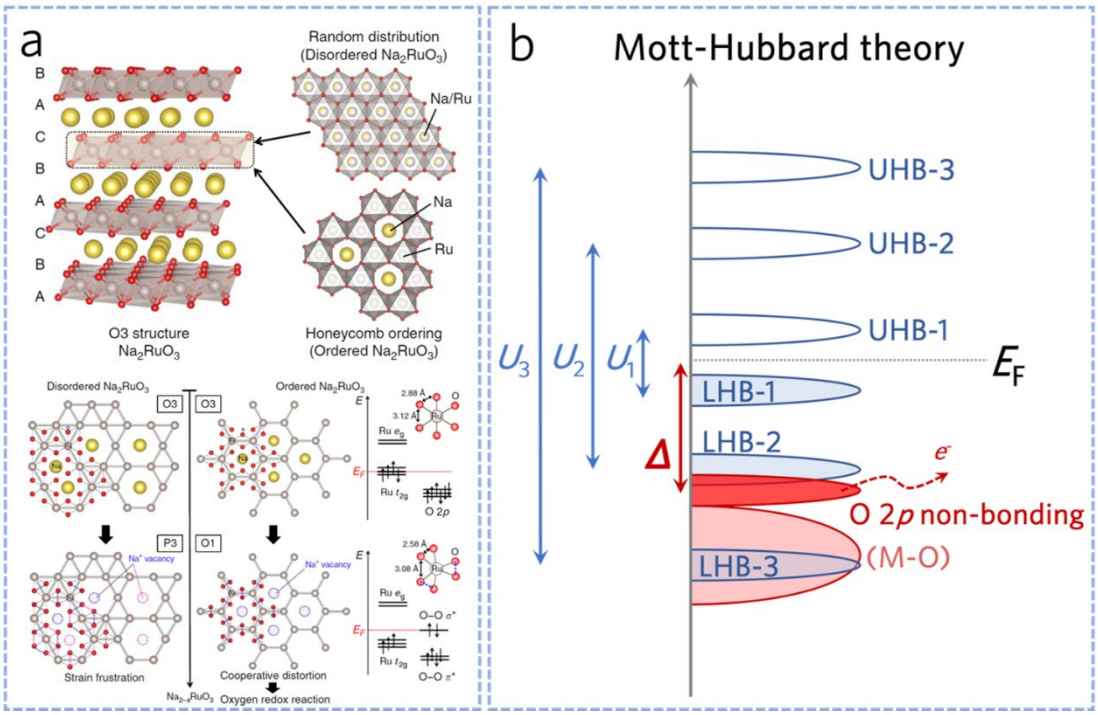

Figure 2 | Discovery of oxygen redox chemistry in layered oxides cathodes for sodium-ions battery. a, Oxygen redox chemistry mechanism in layered Na_2RuO_3. Reprinted from Boisse et al.[33] with permission from Springer Nature. **b**, Classification under three cases of the Li_2MO_3 band structure demonstrating Mott–Hubbard splitting.

With the in-depth investigations on oxygen redox chemistry, the fundamental mechanisms was discussed by Tarascon *et al.* in 2018 [38]. Based on Zaanen–Sawatzky–Allen theory, in energy band structure of layered transition metal oxides, the transition metal (M) *d* orbitals overlap with oxygen (O) *p* orbitals, forming (M—O) bonding and $(M—O)^*$ antibonding. The charge transfer term Δ, representing the energy difference between bonding (M—O) and antibonding $(M—O)^*$, is determined by the

electronegativity difference between M and O. When O is replaced with less electronegativity element, for example S, the charge transfer term Δ decreases as a result of more covalency between transition metal and the ligand. On the other hand, the *d*—*d* Coulomb interaction term *U* is utilized by solid-state physicists to describe the repulsive localized electrons within *d* orbitals [39]. According to Mott-Hubbard theory, this term *U* can split the partially filled $(M—O)^*$ band, forming empty upper-Hubbard bands (UHB) and filled lower-Hubbard bands (LHB). *U* represents the energy difference between UHB and LHB, which decreases from 3*d* to 5*d* transition metals and increases from left to right of the periodic table. Based on the comparison of the values of *U* and Δ, Tarascon *et al.* classified the oxygen redox chemistry into three cases (**Figure 2**b). When $U_1 \ll \Delta$, the (M—O) bonds exhibit highly ionic bonds and electrons are extracted from LHB, resulting in cationic redox only and the oxygen redox cannot be triggered. When $U_3 \gg \Delta$, the energy of O 2*p* band is closer to the Fermi level than LHB, thus the electrons are extracted more easily from O 2*p* than LHB. In this case, the oxygen redox occurs, producing highly reactive O^{n-} species and potentially leading to poor stability and irreversible electrochemical processes. The third case is when $U_2/2 \approx \Delta$ in which the O 2*p* non-bonding band overlaps with LHB, meaning that both of them are active during the redox reaction. The electron extraction results in an unstable degenerate ground state. The degeneracy can be eliminated because the structural distortions can lower the symmetry through shrinking O—O bonds or generating M—$(O_2)^{n-}$ interactions [16]. Therefore, only when the O 2p band center is closer to Fermi level or overlapped with Hubbard band can the oxygen redox occur. Moreover, the reversibility of oxygen redox chemistry largely depends on the stability of M—$(O_2)^{n-}$ interactions. In the designed cathode materials, the Hubbard band and O 2p band can be confirmed by density functional theoretical calculations. According to the values of energy level, the occurrence and reversibility of oxygen redox could be checked.

3. Forms of oxygen redox chemistry

In P-type layered oxides, it has been proved that the specific capacity beyond the

theoretical limit of transition metal redox is attributed to the oxygen activity. With the in-depth study of oxygen redox chemistry, a number of publications reveal the forms or local structure evolutions of P-type cathodes during the charging process. As for P-type cathodes, especially when charged to high voltage, the oxygen redox chemistry could be triggered (**Figure 3**a). It is commonly accepted that, oxygen species during the oxygen redox chemistry could be classified as oxygen electron holes (**Figure 3**b), O—O dimers (**Figure 3**d) and even O_2 molecules (**Figure 3**f), depending on the specific systems.

In P2-typed $Na_{2/3}[Mg_{0.28}Mn_{0.72}]O_2$, Bruce's research group and collaborators proposed the formation of oxygen electron holes during the charge process by performing RIXS characterization. The emission from O 2*p* valence band can influence the spectral weight of O *K*-edge RIXS and the variation of O valance state can be monitored during the charge and discharge process. An obvious change in the spectral weight during the charge process indicates the redistribution of electron density around oxygen site. Recently, Yamada *et al.* also proposed generation of oxygen electron holes, which is (**Figure 3**c) noted as "non-polarizing O redox" [40]. The electron holes could be understood as generation of $O^{(2-n)-}$ species through O^{2-} loses *n* numbers of electron during the charge process.

Formation of O-O dimers is considered as another pathway of the oxygen redox. $[TMO_6]$ octahedra is the basic building block in the crystal structure of the cathode and O—O dimers are generally formed in a distorted $[TMO_6]$ octahedra, which results from the bond distance shrinking of adjacent oxygen atoms. In P3-typed $Na_{0.6}[Li_{0.2}Mn_{0.8}]O_2$, Hu *et al.* utilized the neutron pair distribution function (nPDF) technique to detect the evidence of the formation of peroxo-like O—O dimers with short distance of ~2.506(3) Å after charging (**Figure 3**e)[41]. Combining multi model characterization with DFT calculation, they proposed that the strong covalency of the M-O bond is essential for realizing a reversible oxygen redox process as well as preventing lattice oxygen loss by stabilizing the electrons on oxygen. Furthermore, when several $[TMO_6]$ octahedrons constitute the transition metal layer, the form of oxygen redox could be even O_2 molecules in the crystal structure, which was demonstrated by Bruce's research group

and collaborators in P2-type $Na_{0.67}Mn_{0.72}Mg_{0.28}O_2$. In general, the oxygen oxidation can be demonstrated by O K-edge XAS or RIXS characterizations, but these measurements are not able to provide the quantitative information for formation of O_2 molecules at end of charging. Therefore, Bruce *et al.* performed the Birge-Sponer plot fitting, which can differentiate electron holes, dimers and bulk O_2. As shown in **Figure 3**g, extrapolation of the Birge-Sponer plot gives a fundamental vibrational energy of 0.194 eV, corresponding to 1565(8) cm^{-1}, which is consistent with that of molecular O_2 (1556 cm^{-1}) [42]. This wavenumber is the typical parameter for molecular O_2, which is different from the vibrational frequency of oxygen dimers (O_2^{2-} at ~750 cm^{-1}, O_2^- at ~1100 cm^{-1}) [43]. Moreover, to quantify the O_2 molecules trapped in the bulk of the particles, Bruce *et al.* exploited its paramagnetism with magnetometry measurements (**Figure 3**h). As for O_2^{2-}/ O_2^-/ O^-, they are all diamagnetic so that they would not result in an increase of Curie constant across the high voltage plateau. It clearly shows the gradual rise of the Curie constant until 1.458(9) cm^3 K mol^{-1} at the charged state, estimated to be 10% of the oxide ions in the form of O_2. Based on the multi-model characterization results, origin of O_2 molecules formation is ascribed to displacement of Mg^{2+} into tetrahedral and octahedral sites in the AM layers with equal amounts, which further promotes generation of vacancy-cluster voids that accommodate O_2 molecules. Similar conclusions have been demonstrated by Kang's recent research in P3-type $Na_{0.6}Li_{0.2}Mn_{0.6}Ti_{0.2}O_2$ cathodes [44]. Moreover, Yang *et al.* quantitatively analyzed the reversibility of lattice oxygen redox by advanced mapping of resonant inelastic X-ray scattering with O-*K* super-partial fluorescence yield (noted as mRIXS-sPFY), clarifying the intrinsic properties of lattice oxygen redox activity [45].

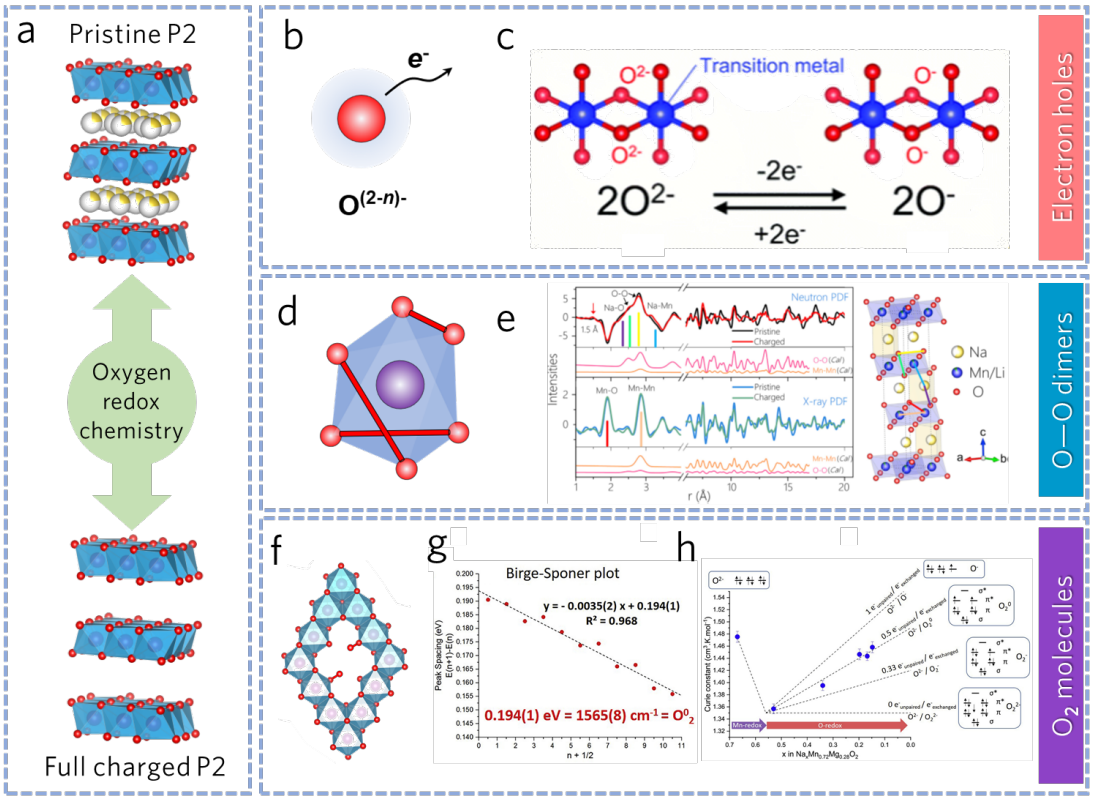

Figure 3 | Different oxygen species formed during oxygen redox processes in P2-type oxides. a, Structure evolution from pristine P2 to full charged P2. Schematic diagrams of **b**, oxygen electron holes, **d**, O—O dimers and **f**, O_2 molecules in crystal structure. **c**, oxygen losing an electron from O^{2-} to O^{-}. Reprinted from Kawai et al[40] with permission from Royal Society of Chemistry. **e**, X-ray and neutron PDF of $Na_{0.6}[Li_{0.2}Mn_{0.8}]O_2$ collected at pristine and charged state (4.5 V). Reprinted from Rong et al[41] with permission from Elsevier **g**, The Birge-Sponer plot of the fully charged P2-$Na_{0.67}Mn_{0.72}Mg_{0.28}O_2$. Reprinted from Boivin et al[42] with permission from Elsevier. **h**, Curie constant as a function of the Na content in $Na_xMn_{0.72}Mg_{0.28}O_2$ measured experimentally (blue dots) and predicted based on different hypothesis for O-redox couples involved: O^{2-}/O^{-} (localized holes), O^{2-}/O_2 (molecular oxygen), O^{2-}/O_2^{2-} (peroxo), and O^{2-}/O_2^{-} (superoxo) represented as black dashed lines. Reprinted from Boivin et al[42] with permission from Elsevier.

4. Issues caused by oxygen redox chemistry

The oxygen redox largely promotes the energy density of the battery through providing a high working potential and extra specific capacity. However, it can also result in several issues such as oxygen loss, voltage hysteresis and capacity decay, severely constrain the electrochemical performance of cathode materials. This section will

discuss three significant issues mentioned above and analyze the major reason with typical examples.

4.1 Oxygen loss

Oxygen loss commonly occurs during the charge process in Li-rich cathode materials. It has been mentioned in the previous literatures that the oxygen loss is closely related to the oxidation state of the oxygen anion as well as stability of the anion species. [24]. To investigate the underlying mechanism of oxygen loss in P2-type cathode materials, Bruce *et al.* performed comprehensive studies on P2-$Na_{0.78}Li_{0.25}Mn_{0.75}O_2$ (NLMO) and P2-$Na_{0.67}Mg_{0.28}Mn_{0.72}O_2$ (NMMO) [46]. The results demonstrated that both of NLMO and NMMO exhibit no oxygen loss at charge cutoff voltage of 4.5 V. When charging at 5.0 V, NLMO exhibit oxygen loss, while NMMO does not. Such a different oxygen redox behaviours of two different cathode materials have been investigated using nuclear magnetic resonance (NMR) online electrochemical mass spectrometry (OEMS) and RIXS characterizations as shown in **Figure 4**. They confirmed that the vacancies in TM layers does not trigger oxygen loss, while high degrees of alkali-ion deficiency (local coordination around oxygen atom below 3) does. When charging NLMO cathode at 5.0 V, Li^+ and Na^+ are extracted out of the structure, resulting in O that is coordinated by only 2Mn. In this case, oxygen loss occurs from the surface of the cathode, further inducing formation of TM densified shell with higher TM/O ratio (similar as Li-rich materials). In comparison, O in NMMO still remains coordinated by 2Mn and 1Mg even at 5.0 V charging due to the sluggish mobility of Mg^{2+}, which is the major reason that the O loss is not observed in NMMO cathode. These findings provide clear understanding for the mechanism of O loss in P-type layered cathode materials and design principle for high capacity cathode materials with reversible O redox processes.

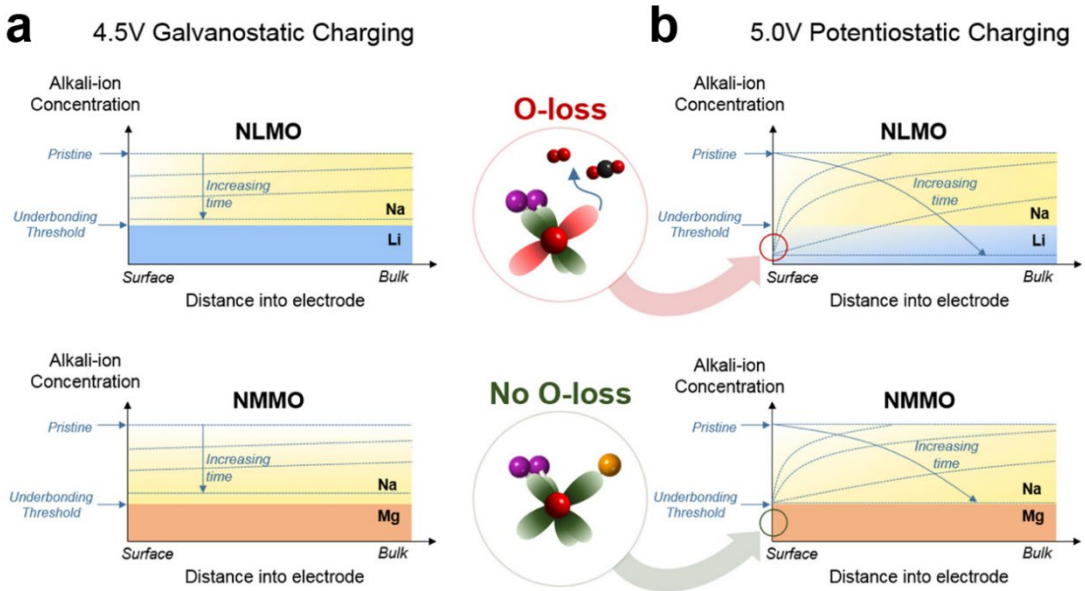

Figure 4 | Schematic representation of the concentration profiles of alkali ions Li, Na, and Mg within P2-$Na_{0.78}Li_{0.25}Mn_{0.75}O_2$ (NLMO) and P2-$Na_{0.67}Mg_{0.28}Mn_{0.72}O_2$ (NMMO) electrode particles as a function of charging time under **a**, 4.5 V galvanostatic and **b**, 5.0 V potentiostatic continuous charging conditions. (**a** and **b**) Reprinted from House et al[46] with permission from American Chemistry Society.

4.2 Voltage hysteresis

Voltage hysteresis is another critical issue in cathode materials with oxygen redox, which has been considered as a significant challenge in Li-rich cathodes [22, 47]. Voltage hysteresis induces low initial coulombic efficiency, irreversible structure evolution and further decreases the energy density. Extensive studies have suggested that voltage hysteresis is attributed to several factors, such as sluggish kinetics of oxygen redox, irreversible TM migration and phase transition as well as asymmetric redox processes etc. Voltage hysteresis is also one of the major roadblocks to development of high energy density P2-type cathodes in SIBs. **Figure 5**a-c demonstrates the charge and discharge galvanostatic three different P2-typed cathodes with oxygen redox process. It can be clearly observed that all of those cathodes suffer from voltage hysteresis but demonstrate different charge/discharge behaviors. The voltage hysteresis can be observed as high as 1.2 V for P2- $Na_{2/3}Mg_{1/3}Mn_{2/3}O_2$ [45],while it is alleviative for P2-$Na_{0.833}Li_{0.25}Mn_{0.75}O_2$ [48] and P2-$Na_{2/3}Zn_{2/9}Mn_{7/9}O_2$ [49]. Recently, the intrinsic reasons for voltage hysteresis have been investigated and

proposed as migration of transition metal ions [42, 44, 50].

Kang's research group analyzed the reasons of asymmetric oxygen redox process and established the relationship among structural disorder, covalent bonding and oxygen redox chemistry [51]. When cation disordering occurs, there is the potential alternation of the density of state (DOS) in the charge and following discharge process (**Figure 5**d). Upon the charging process of the pristine electrode, a typical flat voltage plateau occurs due to the depopulation of the degenerated O 2*p* non-bonding (NB) states. At high oxygen electron holes (h^O), the structural disordering occurs to eliminate the degeneracy of the states, resulting in reorganization of the electronic structure. Meantime, formation of a strong TM-O π hybridization is accompanied by disordering. In the subsequent discharge process, the electrons will fill up the empty M n*d*-O 2*p* π^* state rather than the previous O 2*p* NB state, resulting in redox asymmetry and voltage hysteresis. To investigate the different voltage hysteresis behaviors in several cathodes, Kang *et al.* [51]calculated and compared disorder formation energies. According to the values of h^O among various cathodes, it can be classified into four areas. In the area of NLMO and NMMO, the cations disorder in charge-transfer systems. With the O 2*p* NB states depopulating, the anion and cation disordering show highly spontaneous due to the relatively low Gibbs formation energies ($G_f(M_{Li})$ and $G_f(V_O)$). Meantime, it is very easy for the formation of oxygen dimers to accelerate. Thus, the crystal structure was accompanied by the distortion or even destroy, and the voltage hysteresis show relatively more serious.

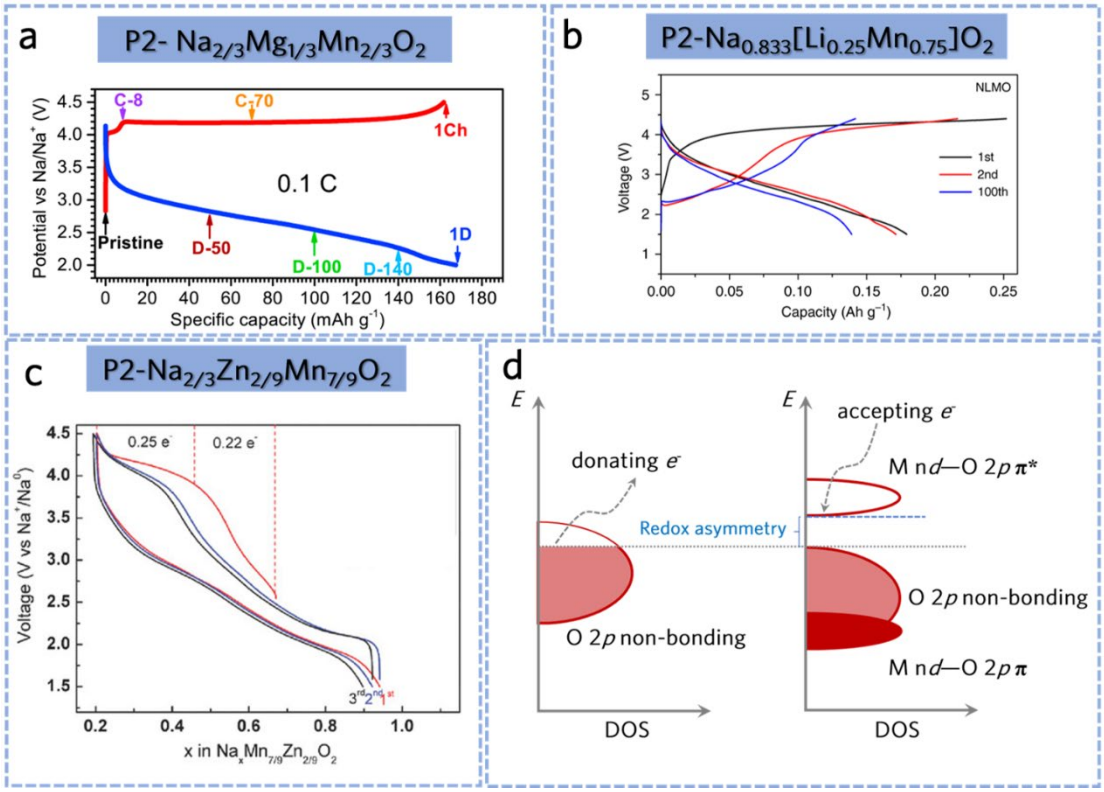

Figure 5 | Voltage hysteresis phenomena and related theoretical studies in P2-type cathodes. The charge and discharge curves of P2-type **a,** $Na_{2/3}Mg_{1/3}Mn_{2/3}O_2$, **b,** $Na_{0.833}Li_{0.25}Mn_{0.75}O_2$ and **c,** $Na_{2/3}Zn_{2/9}Mn_{7/9}O_2$. **d,** Schematic illustration of redox asymmetry arising from cation disordering and consequent strong TM–O π hybridization. **a**, Reprinted from Dai et al. [45] with permission from Elsevier. **b,** Reprinted form Zhang et al[48] with permission from Springer Nature. **c,** Reprinted from Bai et al[49] with permission from Wiley-VCH Verlag.

4.3 Capacity decay

Capacity retention is one of a crucial factor for evaluating the performance of electrode materials. Oxygen loss and voltage hysteresis mentioned above further result in severe capacity decay. Previous studies have highlighted correlation between crystal structure distortion and capacity decay. In other words, local and average structural properties of cathode material including Na^+/vacancy orderings (**Figure 6**a), Jahn-Teller effect of Mn (**Figure 6**b), and irreversible phase transitions (**Figure 6**c) largely affect the cyclic stability of P2-type Mn-based cathode materials. Guo *et al.* investigated the influence of Na^+/vacancy ordering on electrochemical performances of P2-type $Na_{2/3}Ni_{1/3}Mn_{2/3}O_2$ cathode [52]. When the Na content (δ) in cathode is 2/3, there is a large zig zag route between the two nearest Na_f sites. While, Na^+/vacancy ordering

changes from zig zag to one row of Na_f or two rows of Na_e when δ is 1/2. When δ is 1/3, either Na_f or Na_e arranges in rows. Such an in-plane ordering rearrangement of LZZ-row-row results in two voltage plateaus at 3.3 V and 3.7 V, which affects Na^+ diffusion kinetics and leads to capacity decay at a higher current rate. In Mn-based layered cathodes, there is the Mn^{4+}/Mn^{3+} redox upon cycling when the discharge cutoff voltage is 1.5 V. High spin Mn^{3+} (typical for oxides) has the electron configuration of $t_{2g}^3 e_g^1$, which means that there is only one electron in e_g orbitals (including $3d_{x^2-y^2}$ & $3d_{z^2}$). The electrons on $d_{x^2-y^2}$ and d_{z^2} lead to different shielding effects and single occupancy of e_g orbitals would remove the degeneracy through geometric distortion of the octahedra, which is known as Jahn-Teller effect. As for Mn^{4+} with electron configuration of $t_{2g}^3 e_g^0$, the Jahn-Teller effect is absent [53]. To avoid Jahn-Teller distortion induced by trivalent Mn ions, Kang *et al.* optimized the structure of P2-$Na_{0.833}[Li_{0.25}Mn_{0.75}]O_2$ by divalent Zn doping (**Figure 6**b) [48]. As expected, Zn substitution largely alleviates the Jahn-Teller distortion and suppresses the phase transition from P2 to P2'. In general, P-type cathode materials undergo complicate phase transition processes during the charge and discharge, including P2-O2 [54], P2-P'2 [55], P2-OP4 [56] *etc.* Irreversible phase transition due to the incomplete structure evolutions or Na location loss are resulting severe capacity decay as well. Grey *et al.* demonstrated in-depth investigation of the Mg doping effect on the phase transitions of P2-$Na_{2/3}MnO_2$ during the charge and discharge process (**Figure 6**c) [57]. It can be observed that OP4 is formed during Na extraction and P2' is formed during Na reinsertion. Crystal distortion from $P6_3/mmc$ (hexagonal) to *Cmcm* (monoclinic) induces electrochemical performance degradation. In comparison, Mg doping with optimized amount not only alleviates Jahn–Teller distortion by increasing the average oxidation state of Mn but also stabilizes the P2 phase and prevents the OP4 phase formation.

Aside from the structural properties, cathode interfacial chemistry is another culprit for the electrochemical stability of cathode materials at high voltage. When charging at higher cutoff voltage , side reaction between electrolyte and cathode active materials forms cathode electrolyte interface (CEI) [58]. Meanwhile, the stability of CEI is

closely related to the electrochemical performance of electrode materials. Unstable CEI induces undesirable parasitic reaction, which facilitates consumption of electrolyte and active materials. As a typical example, Zhang *et al.* systematically studied the relationship between CEI stability and cycling performance of P2-$Na_{2/3}Ni_{1/3}Mn_{2/3}O_2$, [59]. The cathode cycled in fluoroethylene carbonate (FEC) based electrolyte demonstrates enhanced cyclic and rate performances than that of propylene carbonate (PC) based electrolyte due to FEC molecule is more stable at cathode site. According to EIS results, it can be observed that the interfacial resistances of the cells cycled in FEC electrolyte decreases with increasing cycles, while interfacial resistance increases gradually in PC based electrolyte (**Figure 6**d). Zhang *et al.* proposed that the FEC electrolyte forms a robust and F-rich CEI, effectively passivates electrode surface and prohibit further decomposition of electrolyte (**Figure 6**e). However, aggressive side reaction in PC based electrolyte results in a thick CEI layer that induces sluggish Na^+ kinetics and accelerated capacity decay. At the same time, as illustrated in schematic diagram of **Figure 6**e, the unstable CEI also leads to Li/TM dissolutions and serious structural degradation [60]. Hu *et al.* investigated the Li/Mn dissolutions in the conventional and highly fluorinated electrolytes [61]. They utilized advanced electron paramagnetic resonance (EPR) spectra (**Figure 6**f) to show fewer Mn loss from $Na_{0.66}[Li_{0.22}Mn_{0.78}]O_2$ cathode in highly fluorinated electrolyte. The ICP results (**Figure 6**g) also indicates 6.5 times decrease in the content of dissolved Mn with highly fluorinated electrolyte. They proposed that the dissolved Mn could even deposit on the anodes, leading to the adverse effect on the coulombic efficiency.

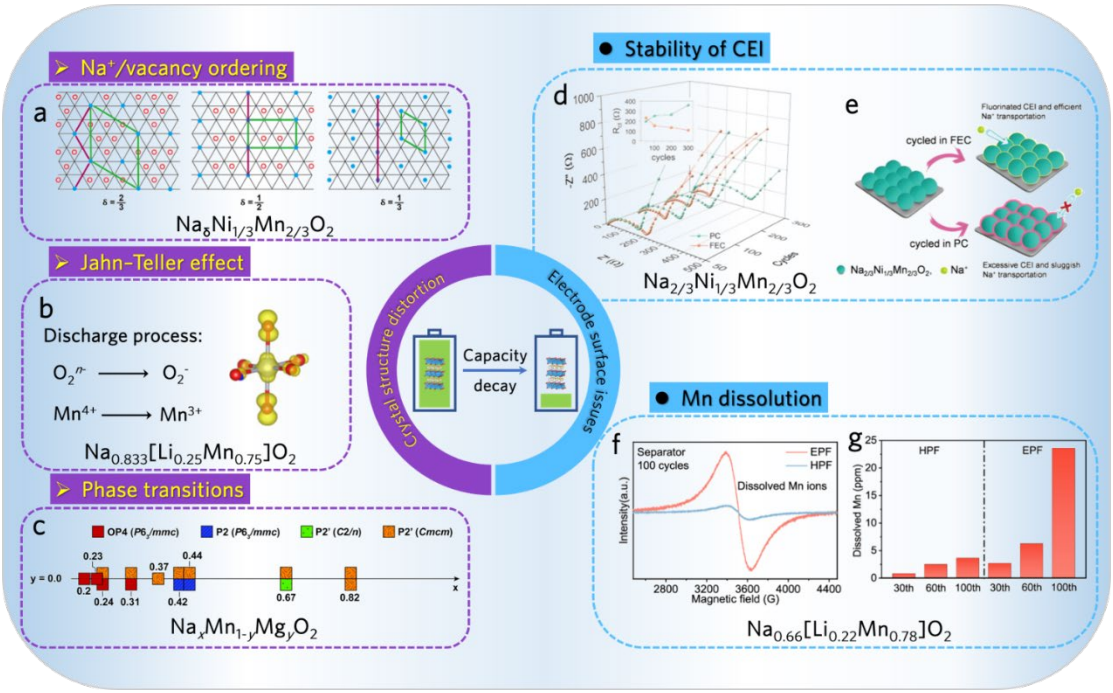

Figure 6 | Typical reasons for the capacity decay of Mn-based layered oxides. a, In-plane Na^+/vacancy orderings of $Na_\delta Ni_{1/3}Mn_{2/3}O_2$ in the triangular lattice at $\delta = 2/3$, $\delta = 1/2$, and $\delta = 1/3$, respectively (empty red circles, Na^+ on Na_e sites; solid blue circles, Na^+ on Na_f sites; thick green lines, unit cell). **b,** Jahn-Teller effect of Mn^{3+} in $Na_{0.833}[Li_{0.25}Mn_{0.75}]O_2$ in the discharge process. **c,** Ranges of P2, P2' and OP4 phase stability for $Na_xMn_{1-y}Mg_yO_2$ ($y = 0.0$) upon electrochemical Na removal and reinsertion. **d,** The Nyquist curves of electrodes after 50, 100, 200, and 300 cycles at 5 C in FEC and PC electrolytes. The inset summarizes the charge transfer resistances of the electrodes after different cycles. e) Schematic illustration of the CEI formation on $Na_{2/3}Ni_{1/3}Mn_{2/3}O_2$ grains after cycling in FEC and PC electrolytes. f) EPR spectra of the separators extracted from the coin cells cycled with EPF and HPF after 100 cycles. g) ICP results for the dissolved Mn content after 100 cycles. **a,** Reprinted from Wang et al[52] with permission from American Association for the Advancement of Science. **b,** Reprinted from Zhang et al[48] with permission from Springer Nature. **c,** Reprinted from Clement et al[57] with permission from Royal Society Chemistry. **d** and **e**, Reprinted from Wu et al[59] with permission from Wiley-VCH Verlag. **f** and **g**, Reprinted from Zhao et al[61] with permission from American Chemistry Society.

5. Strategies to improve oxygen redox

Sodium layered oxides with oxygen redox chemistry have opened new directions for developing high energy density battery systems. However, as summarized in the previous section, oxygen loss, voltage hysteresis and capacity fade induced by oxygen redox hinder the development of high-capacity cathode materials. Tremendous efforts

have been made to circumvent these limitations, including superlattice construction, element substitution, and surface modification. In this section, effectiveness of different strategies and underlying mechanism will be discussed in detail.

5.1 Superlattice engineering

Substitution of other elements in Mn layer induces formation of superlattice ordering in P-type layered cathode, which can be reflected as a small peak on XRD patterns. As mentioned in research work published by Bruce's group and collaborators, the superlattice was proposed to have an effect on the voltage hysteresis of P2-type $Na_{0.6}Li_{0.2}Mn_{0.8}O_2$ [62]. To clarify underlying mechanism, P2-$Na_{0.75}Li_{0.25}Mn_{0.75}O_2$ with honeycomb superlattice and P2-$Na_{0.6}Li_{0.2}Mn_{0.8}O_2$ with ribbon superlattice have been constructed. The ribbon arrangement shows the structural repeating unit includes one Li atom and four Mn atom, in which the superlattice is represented as $LiMn_4$ ribbon. During the initial discharge process, the honeycomb structure exhibits obvious voltage loss but the ribbon structure does not. At the same time, the oxygen redox plateau of the ribbon structure maintains at 4.0 V in the discharge process, indicating the ribbon structure largely promotes the discharge voltage of P2-type Na-Li-Mn-O cathodes. Based on the characterization result, it has been proposed that the Li migrates out of plane to the alkali layer, while Mn migrates in plane to the Li-vacancy during the charge process. For the ribbon structure, the Li vacancies are more dispersed in contrast to the honeycomb structure, therefore, the Mn migration is suppressed, which is stabilizing electron holes on O^{2-} and preventing formation of O_2. As a result, ribbon structure exhibits enhanced stability of high voltage oxygen redox by suppressing the degeneracy of the O 2*p* states. Effectiveness of superlattice engineering on electrochemical behavior of cathode materials has been also verified in $Na_2Mn_3O_7$ cathodes with a mesh structure, which has been reported with more dispersed vacancies and higher reversibility of high-voltage oxygen redox plateau [63]. After Bruce's research work, Pan *et al.* constructed the $MgMn_6$ honeycomb superstructure in P2-$Na_{0.73}Li_{0.11}Mn_{0.12}Mg_{0.77}O_2$ [64] with strong Mg^{2+}—O^{2-} interaction (**Figure 7**a), in

which the O 2*p* of Na-O-Mg state is in the middle of Na-O-Li and Na-O-Mn (**Figure 7**b). During the charge process, the Mg^{2+} can suppress the Mn ion migration and stabilize the structure of TM layer (**Figure 7**c).

Constructing dual superlattice has positive effect on tuning the electrochemistry of cathode materials as well. In a recent study done by Zhou *et al.*, dual honeycomb superlattice of $LiMn_6$-$MgMn_6$ has been constructed in P2-type $Na_{2/3}[Li_{1/7}Mn_{5/14}][Mg_{1/7}Mn_{5/14}]O_2$ cathode [65]. As shown in **Figure 7**d, each $LiMn_6$ unit is adjacent to a $MgMn_6$ unit in the dual honeycomb superlattice. The capacity retention of cathode with such a special superlattice is as high as 85.5% at 1C (100 mA g^{-1}) after 50 cycles. To further understand the mechanism of the special superlattice, Zhou *et al.* performed ^{7}Li NMR spectra of the sample collected at different SOCs of the first cycle (**Figure 7**f). In charge process, the NMR spectrum shows a new broad resonance (Li_{AM2}) at the right side of the 750 ppm (Li_{AM1}) peak, indicating Li^+ migrate out of plane from the TM layer to the Na layer which is consistent with results shown in Na-Li-Mn-O cathode [62]. At discharge state, it can be obviously observed that the Li^+ in $LiMn_6$-$MgMn_6$ could return to Li_{TM1} sites in the TM layer, demonstrating the reversible migration of Li^+ in the dual superlattice. Zhou *et al.* proposed that the Mg^{2+} in the dual superlattice serve as pillars when Li^+ migrate out of plane, retaining the stability of the honeycomb superlattice (**Figure 7**g). The cation migration during the electrochemical process induces the formation superlattice, resulting in a voltage hysteresis and the irreversibility of the oxygen redox. Constructing a stable superlattice to relive the negative effect of cation migration is of great significance.

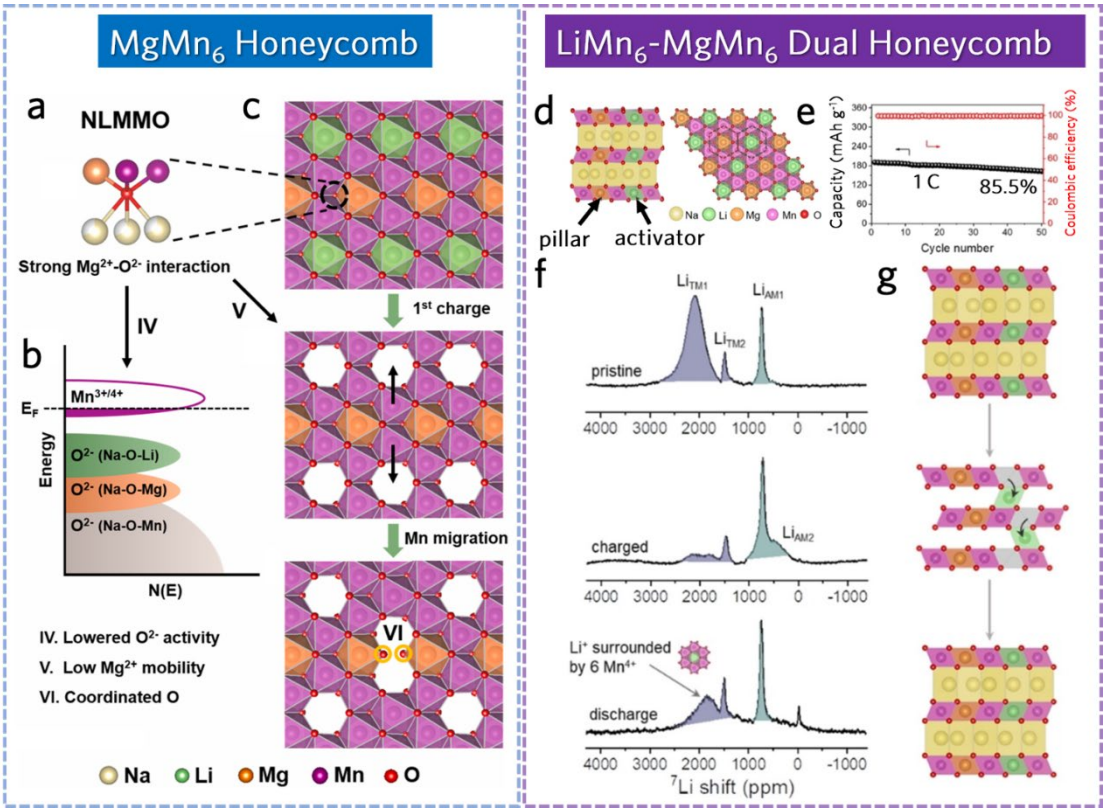

Figure 7 | Electrochemical performance improvements by constructing superlattice. **a,** Local coordination environments of NLMMO. **b,** Schematic illustrations for O 2p DOS. **c,** Schematic illustration of the in-plane structural evolutions of NLMMO during the first charge. **d,** Dual honeycomb superlattice of P2-$Na_{2/3}[Li_{1/7}Mn_{5/14}][Mg_{1/7}Mn_{5/14}]O_2$. **e,** Cycling performance of P2-$Na_{2/3}[Li_{1/7}Mn_{5/14}][Mg_{1/7}Mn_{5/14}]O_2$ at 1 C (100 mA g^{-1}). **f,** ^{7}Li NMR spectra collected at different stages of the first cycle for P2-$Na_{2/3}[Li_{1/7}Mn_{5/14}][Mg_{1/7}Mn_{5/14}]O_2$. **g,** Layer stacking schematic at different states for P2-$Na_{2/3}[Li_{1/7}Mn_{5/14}][Mg_{1/7}Mn_{5/14}]O_2$. (**a, b** and **c**) Reprinted from Liu et al.[64] with permission from Elsevier. (**d, e, f** and **g**) Reprinted from Wang et al.[65] with permission from Wiley.

5.2 Elemental substitution

Elemental substitution into layered oxides is the most common strategy to improve the stability of crystal structure. Different dopants have different effects on structural stability and overall performances of cathode materials due to their distinct physical properties. At present, the element substitution approach can be classified into four categories. A dopant with smaller ion radius, boron for example, can be only doped in the interstitial void, which is called lattice doping. An element with larger atom size is substituted in the TM layer or AM layer (for example, Li^+, Mg^{2+}, Ti^{4+}, *et al*) rather than

interstitial void, which is AM/TM layer substitution. For the case of AM layer substitution, TM layers could not accommodate the element with large ionic radius, therefore, can only be located in AM layer (for example, K^+, Ca^{2+}, *etc.*). The last one is vacancy substitution, in which defects/vacancies are constructed in TM layer.

Zhou *et al.* have introduced Mg^{2+} into P2-type $Na_{0.8}Mn_{0.6}Co_{0.4}O_2$ in their recent research work to enhance the structural stability [66]. XRD and NPD characterizations have been conducted and the results demonstrated Mg ions are locating in both AM layer (Na sites) and TM layer (TM sites), inducing formation of native TM vacancies (**Figure 8**a). DFT calculation results suggested that the vacancies near the oxygen atoms can influence the electron density of the O atoms, resulting in a deflection to the vacancy location (black arrow in **Figure 8**b). Moreover, the energy level of Mg 3*s* states are relatively high with O 2*p*, leading to form weak and ionic Mg—O bonds and promoting the energy level of O 2*p* states (**Figure 8**c). Benefitting from the native vacancy substitution, the P2-$Na_{0.8}Mg_{0.13}[Mn_{0.6}Co_{0.2}Mg_{0.07}\square_{0.13}]O_2$ exhibits the high capacity retentions of 89.9% and 81.7% after 150 cycles at 4 C and 10 C, respectively (**Figure 8**d). The vacancy substitution enhances the flexibility of the crystal structure, which has been verified again in P2-type $Na_{0.7}Mg_{0.2}[Fe_{0.2}Mn_{0.6}\square_{0.2}]O_2$ cathode by Zhou's research group and collaborators [67]. In the latest research, Liu et al. developed P2-$Na_{0.80}Li_{0.08}Ni_{0.22}\square_{0.03}Mn_{0.67}O_2$ cathode, where the oxygen redox activity was stimulated by TM vacancy and Li [68].

Boron substitution has been verified as an effective strategy for enhancing structural/interphasial chemistry of cathode materials. Vaalma *et al.* attempted to stabilize the structure of P2-type $Na_{2/3}MnO_2$ by B-doping and the $Na_{2/3}B_{0.11}Mn_{0.89}O_2$ enhanced the average potential and exhibited good rate performance [69]. Guo *et al.* successfully developed a doping strategy that introducing boron into the interstitial void in O3-$NaLi_{1/9}Ni_{2/9}Fe_{2/9}Mn_{4/9}O_2$ crystal structure (**Figure 8**e) [70]. DFT calculations demonstrated that the boron and its adjacent O atoms form a strong-covalent B—O bond (**Figure 8**f), resulting in more electronically negativity of O atom to suppress excessive oxidation upon charging beyond 4.0 V. As expected, the B-doped $NaLi_{1/9}Ni_{2/9}Fe_{2/9}Mn_{4/9}B_{1/50}O_2$ exhibited excellent cycling stability at 250 mA g^{-1} with a

capacity retention of 82.8% after 200 cycles (**Figure 8**g).

Substitution of electrochemically inactive cations (for example, Li^+, Mg^{2+}, Ti^{4+}, *et al*) in AM/TM layers can effectively modify the crystal and electronic structures of cathode materials. Among the various cation dopants, Mg^{2+} is a special one because it has been reported to be introduced in both AM layer and TM layer [71, 72]. Zhou *et al.* successfully introduced Mg^{2+} into Na sites of P2-type $Na_{0.7}[Mn_{0.6}Ni_{0.4}]O_2$ in addition to the conventional TM sites (**Figure 8**h) [71]. They proposed that Mg^{2+} in Na sites could serve as "pillars" to promote the stability of the layered structure and Mg^{2+} in TM layer could destroy charge ordering. Therefore, kinetics and cycling performance of the cathode have been improved obviously. Different from Mg^{2+}, Ti^{4+} can only be introduced in TM layer. Hu *et al.* reported a Ti-substitute P2-type $Na_{2/3}Mg_{1/3}Ti_{1/6}Mn_{1/2}O_2$ cathode with facilitated the oxygen oxidation [73]. As demonstrated in results Mg, Ti, and Mn ions are located in two octahedral sites in TM layer (**Figure 8**i). In addition, Ti substitution can promote the structural stability during cycles by breaking Mn and Mg ordering distribution due to the intermediate ion size of Ti^{4+}. Furthermore, they proposed that introducing Ti^{4+} also can localize electrons around oxygen ions and promote the reversible oxygen redox chemistry. Thus, the P2-type $Na_{2/3}Mg_{1/3}Ti_{1/6}Mn_{1/2}O_2$ cathode exhibited a very high reversible capacity of 230 mAh g^{-1} and excellent cycling performance (**Figure 8**j). In the latest research, Liu et al. developed P2-$Na_{0.8}$0$Li_{0.08}Ni_{0.22}\square_{0.03}Mn_{0.67}O_2$ cathode, where the oxygen redox activity was stimulated by TM vacancy and Li [74].

K^+ with large ionic radius of 138 pm has been reported by Li *et al.* to be introduced in the prismatic Na^+ sites of P2-type $Na_{0.612}K_{0.056}MnO_2$ cathode to enable more favorable Na^+ vacancies [75]. In the K^+ introduced structure (**Figure 8**k), K^+ is located at the Na_e sites and the interlayer space is enlarged to 3.58 Å *vs*. $Na_{0.706}MnO_2$ (3.42 Å). As a result, the strengthening of Na—O bond and reduction of Na^+ vacancy formation energy facilitate insertion/extraction of Na^+. Therefore, the improved cathode exhibited a very high reversible capacity of 240.5 mAh g^{-1} and high capacity retention of 98.2% at 50 mA g^{-1} after 100 cycles (**Figure 8**l). Similar to the benefit of K^+, Ca^{2+} has been reported recently to be introduced into the AM layer and enlarge the interlayer space of

the crystal structure [76, 77]. Liu *et al,* reported a Ca-introduced P2-$Na_{0.75}Ca_{0.05}Li_{0.15}Fe_{0.2}Mn_{0.6}O_2$ cathode, in which Ca ions occupy both Na_f and Na_e sites (**Figure 8**m), while other TMs Fe/Mn/Li are distributed in the octahedral sites of TMO_2 slabs. They proposed that Ca^{2+} can serve as "pillars" to suppress the gliding of TM layers, inhibit the Na^+/vacancy ordering, and prevent the oxygen loss by the formation of strong Ca—O bonds. Furthermore, the Ca-doped cathode shows the excellent cycling performance at 1C (220 mA g^{-1}) with a capacity retention of 76% after 150 cycles (**Figure 8**n).

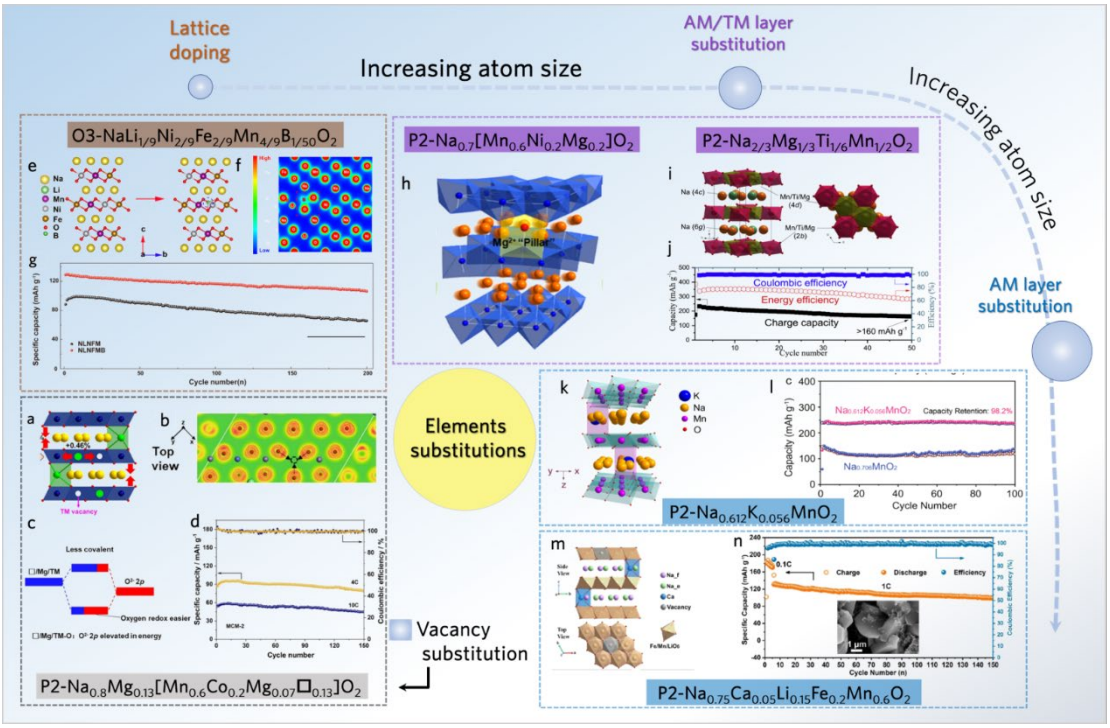

Figure 8 | Classification of elements substitution in layered Mn-based transition metal oxides. a, Crystal structure of P2-$Na_{0.8}Mg_{0.13}[Mn_{0.6}Co_{0.2}Mg_{0.07}\square_{0.13}]O_2$. **b,** Top view of the electron localization functions (ELF) in $Na_{0.8}Mn_{0.6}Co_{0.2}Mg_{0.2}O_2$. **c,** Schematic illustration of the electron energy level diagrams of the Mg/□ containing TM *d*-O 2*p* bonding interactions. **d,** Cycling performance of $Na_{0.8}Mn_{0.6}Co_{0.2}Mg_{0.2}O_2$. **e,** Crystal structure, **f,** Contour maps of charge density on corresponding planes and **g,** cycling performance at 250 mA g^{-1} of O3-$NaLi_{1/9}Ni_{2/9}Fe_{2/9}Mn_{4/9}B_{1/50}O_2$. **h,** Crystal structure of P2-$Na_{0.7}[Mn_{0.6}Ni_{0.2}Mg_{0.2}]O_2$. **i,** Crystal structure and **j,** cycling performance at 40 mA g^{-1} of P2-$Na_{2/3}Mg_{1/3}Ti_{1/6}Mn_{1/2}O_2$. **k,** Crystal structure and **l,** cycling performance at 50 mA g^{-1} of P2-$Na_{0.612}K_{0.056}MnO_2$. **m,** Crystal structure and **n,** cycling performance at 1 C (220 mA g^{-1}) of P2-$Na_{0.75}Ca_{0.05}Li_{0.15}Fe_{0.2}Mn_{0.6}O_2$. (**a, b, c** and **d**) Reprinted from Li et al[66] with permission from Wiley. (**e, f** and **g**) Reprinted from Guo et al.[70] with permission from Springer Nature. h, Reprinted from Wang et al.[71] with permission from American Chemistry Society. **i** and **j**, Reprinted from Zhao et al.[73] with permission

from Elsevier. **k** and **l**, Reprinted from Wang et al.[75] with permission from Springer Nature. **m** and **n**, Reprinted from Wang et al.[76] with permission from Elsevier.

5.3 Other strategies

In order to realize higher energy density, P2-type layered oxides cathodes can be charged beyond 4.2 V. However, with the voltage promoting, the electrolyte is tending to decompose on the cathode surface. The cathode-electrolyte interface (CEI) is unstable at high voltage, which is resulting in continuous electrolyte decomposition, surface reconstruction, transition metal dissolution and further capacity decay [78]. Thus, improve the stability of CEI is significant and the strategies can be classified as artificial CEI construction, surface modification, electrolyte composition regulation. Yang's research group and collaborators recently has reported a simple but effective water-mediated strategy to synthesize a shale-like Na_xMnO_2 (S-NMO) cathode [79]. They realized insertion of H_2O molecules into Na^+ layer, which can enlarge the interlayer space (**Figure 9**a). In the subsequent process, nanoflake S-NMO with high purity could be obtained by removing H_2O through heating process. Such a modified S-NMO exhibited outstanding cycling stability at 96 mA g^{-1} with 83% capacity retention after 3000 cycles (**Figure 9**b).

Surface modification approaches have been suggested to improve the overall performance of electrodes, which is mainly realized by constructing the secondary structures for cathode particles. Constructing special morphologies of the particles and building a protective layer are the common ideas. CEI stability In terms of building the protective layer, it mainly tackles the unfavorable issues form the electrolyte [58]. Wang *et al.* [80] reported effectiveness $NaTi_2(PO_4)_3$ (NTP) surface coating on interfacial stability of P2- $Na_{0.67}Ni_{0.33}Mn_{0.67}O_2$ cathode with Mg substitution (**Figure 9**c). With NTP surface modification, the cathode exhibits promoted cycling stability at 1 C (173 mA g^{-1}) with 77.4% capacity retention after 200 cycles (**Figure 9**d). For the pristine $Na_{0.67}Ni_{0.33}Mn_{0.67}O_2$ cathode, there is the formation of HF in the reaction of electrolyte salts with H_2O molecules, leading to the serious particle crack and degeneration. It is proposed that the NTP coating can stabilize the interface by inhibiting the HF attack,

which is further facilitating Na^+ migration at cathode-electrolyte interface.

Focusing on electrolyte composition regulation, Zhang *et al*. developed an electrolyte based on sodium bis(fluorosulfonyl)imide (NaFSI)–triethyl phosphate (TEP) to stabilize the CEI and optimize the performance at high voltage [78]. By substituting with TEP, the thickness of CEI could be largely deceased to 7 nm while the thickness in PC was observed to be 16 nm, resulting in the reduction of interfacial resistance (**Figure 9**e and f). Benefiting from the TEP electrolyte, the full cell assembled with hard carbon and $NaNi_{0.68}Mn_{0.22}Co_{0.10}O_2$ exhibited promoted capacity retention of 83.5% for 200 cycles at 0.2 C (1C = 200 mAh g^{-1}) (**Figure 9**g).

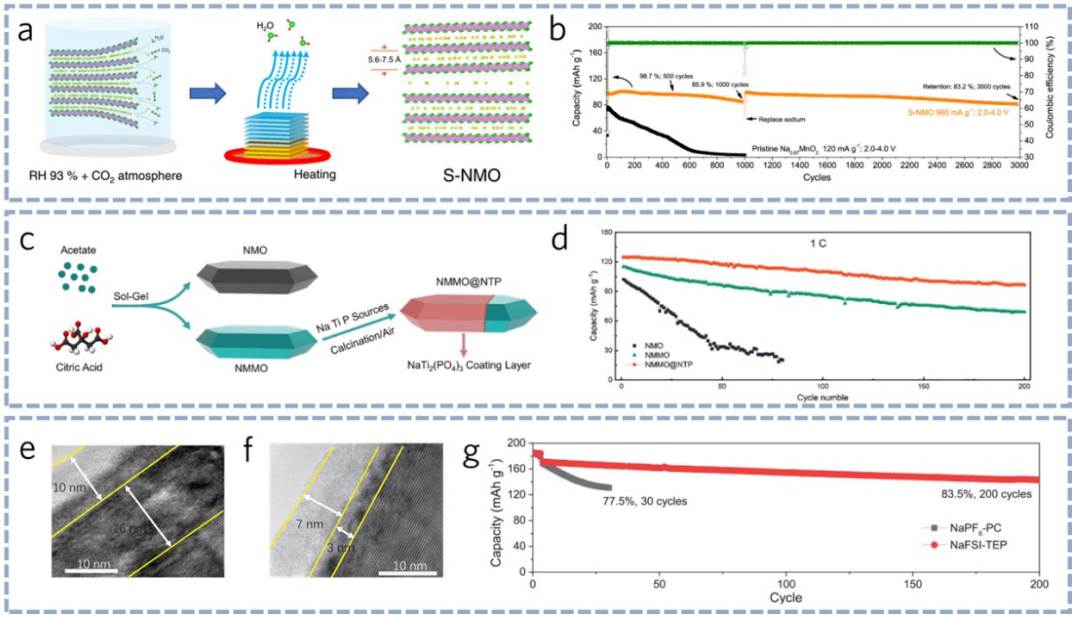

Figure 9 | Other strategies of improving layered oxides. a, Process of the water-mediated strategy for $Na_{0.67}MnO_2$. **b,** comparison of the cycling performance of pristine $Na_{0.67}MnO_2$ and S-NMO electrodes at 960 mA g^{-1}. **c,** Schematic illustration for NTP modification. **d,** Cycling performance comparison of NMMO@NTP electrodes at 1 C (173 mA g^{-1}). Cryo-TEM images of cathode surfaces after 50 cycles in (**e**) $NaPF_6$-PC and (**f**) NaFSI-TEP electrolytes. **g**, Long-cycling performance of hard-carbon||NaNMC full cells in two electrolytes. (**a** and **b**) Reprinted from Zuo et al. [79]with permission from Springer Nature. (**c** and **d**) Reprinted from Tang et al. [80] with permission from Elsevier. (**e**,**f** and **g**) Reprinted from Jin et al. [78]with permission from Wiley.

6. Summary and prospects

In recent years, sodium-ion batteries have been regarded as the most promising

alternatives to lithium-ion batteries due to the similar properties as well as higher abundance of Na [81, 82]. It is very urgent and important to develop SIBs cathodes with high energy density to promote the practical applications. Layered oxides with oxygen redox chemistry display enormous prospect in the next generation cathodes by providing extra capacity and high potential of oxygen redox [83, 84]. Na-O-A/A', Na-O-V or V'-O-A/A' (A is alkaline metal (Li/Na) A' is TMs that do not hybridize with oxygen 2p orbital; V and V' are TM vacancy and Na vacancy, respectively) are attributed to the ORR in cathode materials. For P2 type layered cathode material with Li/Mg or vacancy substitution, both Li/Mg/V'-O-Na/V configurations promote ORR by forming nonbonding O 2p states and lone-pair O electrons. In addition, it is also proposed that ORR can be stabilized in P type structure but it is irreversible in the O-type structure. The homogenous distortion of O networks in P2-type cathodes allow O-O pairings have equivalent oxidation states, which further alleviates the O2 release. However, for the O-type cathode materials, cation migration induces disproportion of oxygen to O_2^- and peroxo-like $(O_2)^{2-}$, which is resulting the oxygen loss. However, the issues caused by oxygen redox are also difficult to be tackled because of the complex structure evolutions and the puzzled ion migration. Thus, it is critical to provide timely update of recent progress to comprehensively understand oxygen redox chemistry. This review systematically illustrates the development of oxygen redox chemistry in SIBs, including its discovery, theoretical model, typical forms, critical issues, and corresponding solutions.

The utilization of oxygen redox chemistry in layered cathode materials is by far demonstrated to be promising, however, challenges still remain before they can be successfully utilized at practical conditions. Several future directions require further attention as mentioned below.

(i) Elemental substitution may be the most convenient way to improve the electrochemical performance, as has been widely attempted in layered oxides cathodes (**Table 1**). Introducing the elements into transition metal layers can regulate the oxygen electronic orbitals, generating robust [TMO6] and improving the cyclic stability. Element substitution in alkali metal layer can

serve as the “pillar”, which can stabilize the layered structure and suppress the phase transition. Therefore, the elemental substitution is the most feasible way to improve cycling performance of cathode materials with ORR. For example, Ti substitution is one of the effective strategies for enhancing cyclic performances of cathode materials with ORR by improving the structure of cathode materials[85]. In the future study, the effectiveness of electronic structure, ionic radius, atomic location of elements on the electrochemical performance of cathode materials should be systematically investigated. Typically, the different atom sizes can have an obvious impact on the doping sites. For example, B can be doped in the interstitial void for its very small radius. But K^+/Ca^{2+} can only be located in the interlayer for the very large radius. Substitution of elements with different ionic radius and electronegativity demonstrates various impact on the overall performances of cathode materials with ORR. Therefore, the relationship between the properties of substituents and the electrochemical performances of cathode materials should be clarified, which provides valuable insight into design a novel cathodes with high performance.

(ii) Three typical forms of oxygen redox chemistry have been discussed, including oxygen electron holes, O—O dimers, and O_2 molecules. These forms were characterized by sophisticated techniques such as the RIXS, XAS, Raman spectroscopy, EPR, *et al*. It is very important to select the appropriate characterizations to investigate bulk oxygen redox [86, 87]. For example, Lab-XPS is a surface sensitive technique and utilized to detect surface information, while synchrotron hard X-ray Photoelectron Spectroscopy (HAXPES) can provide bulk information. In addition, bulk sensitive techniques such as hard/soft XAS, RIXS, synchrotron/neutron PDF and *in-situ* Raman spectroscopy are also utilized to analyze bulk charge compensation mechanism. However, during the oxygen redox process, there is no definite demonstration whether the three forms can transform from one to the other. More specifically, what is the correlation among the oxygen electron holes, O—O dimers and O_2

molecules? What is the order of generation of the three oxygen forms? These questions are rarely mentioned in other studies but critical for understanding the ORR mechanism. In the previous studies, the unified point of the relationship among three oxygen products is still a controversy. As mentioned above, they are the three forms in different dimensions such as the oxygen electron hole, oxygen dimmer and molecular O_2 are focused on oxygen atom, [TMO_6] octahedron and transition metal layer, respectively. Therefore, development of *in-situ* diagnostic techniques is essential to reveal the relationship among the three forms.

(iii) As mentioned in the previous section, the voltage hysteresis is one of the serious issues caused by oxygen redox chemistry. While the factors contributing to voltage hysteresis are complex. Bruce's group and collaborators demonstrated that it is possible to mitigate the voltage hysteresis by constructing the ribbon superstructure. In addition, the sluggish kinetics of oxygen redox is another hurdle that needs to overcome.

(iv) The properties of the interface between cathodes and electrolyte are crucial to the battery performance as mentioned by Xu et al. [58, 88]. The oxygen redox in SIBs usually occurs beyond 4.0 V, therefore, the stability of CEI should be considered. Electrolyte engineering such as tuning the solvation structure by screening novel solvents and introducing film-forming additives is one of the effective strategies to form stable CEI. In addition, surface coating is also effectively preventing surface side reaction, but the thickness should be optimized carefully.

(v)

Table 1 Summary of different strategies to improve the performance of P2-type cathodes.

Strategies	Cathode materials	Current density/mA g-1	Initial capacity/mAh g^{-1}	Voltage range/V	Cycle number	Capacity retention	Ref
Superlattice	$Na_{0.6}Li_{0.2}Mn_{0.8}O_2$	10	115	2.0-4.5	——	——	[62]
engineering	$Na_{2/3}[Li_{1/7}Mn_{5/14}][Mg_{1/7}Mn_{5/14}]O_2$	100	190	1.5-4.5	50	85.5%	[65]
Vacancy	$Na_{0.8}Mg_{0.13}[Mn_{0.6}Co_{0.2}Mg_{0.07}\square_{0.13}]O_2$	680	90	1.5-4.5	150	89.9%	[66]
substitution	$Na_{0.80}Li_{0.08}Ni_{0.22}\square_{0.03}Mn_{0.67}O_2$	23.4	120	2.0-4.3	50	94.8%	[68]

B doping	$NaLi_{1/9}Ni_{2/9}Fe_{2/9}Mn_{4/9}O_2$	250	125	2.0-4.5	200	82.8%	[70]
Mg substitution	$Na_{0.7}Mg_{0.05}[Mn_{0.6}Ni_{0.2}Mg_{0.15}]O_2$	170	73	2.5-4.2	1000	79%	[71]
	$Na_{0.773}Mg_{0.03}Li_{0.25}Mn_{0.75}O_2$	20	135	2.6-4.5	100	57.8%	[72]
Ti substitution	$Na_{2/3}Mg_{1/3}Ti_{1/6}Mn_{1/2}O_2$	40	230	1.5-4.5	50	69.5%	[73]
Cu substitution	$Na_{0.8}Cu_{0.22}Li_{0.08}Mn_{0.67}O_2$	26	122	2.0-4.4	50	90.3%	[74]
K substitution	$Na_{0.612}K_{0.056}MnO_2$	50	240	1.8-4.5	100	98.2	[75]
Ca substitution	$Na_{0.75}Ca_{0.05}Li_{0.15}Fe_{0.2}Mn_{0.6}O_2$	220	130	1.5-4.3	150	76%	[76]
	$Na_{0.75}Ca_{0.04}[\square_{0.03}Li_{0.1}Ni_{0.2}Mn_{0.67}]O_2$	1070	80	2.0-4.3	500	87.7%	[77]
Interlayer spacing engineering	$Na_{0.67}MnO_2$	960	100	2.0-4.0	3000	83.2%	[79]
$NaTi_2(PO_4)_3$ surface modification	$Na_{0.67}Ni_{0.33}Mn_{0.67}O_2$	173	123	2.5-4.3	200	77.4%	[80]
electrolyte composition regulation	$NaNi_{0.68}Mn_{0.22}Co_{0.10}O_2$	66	160	2.0-4.2	500	81%	[78]

Acknowledgement

The work at Shanghai Jiao Tong University was financially supported by the National Natural Science Foundation of China (No. 22209106) and Shanghai Pujiang Program (21PJ1408700). The work at Brookhaven National Laboratory was supported by the Assistant Secretary for Energy Efficiency and Renewable Energy (EERE), Vehicle Technology Office (VTO) of the US Department of Energy (DOE) through the Advanced Battery Materials Research (BMR) Program under contract no. DE-SC0012704.

References:

[1] B. Dunn, H. Kamath, J.-M. Tarascon, Science 334 (2011) 8.

[2] Y. Lu, C.-Z. Zhao, J.-Q. Huang, Q. Zhang, Joule 6 (2022) 1172-1198.

[3] J. Liu, J. Xiao, J. Yang, W. Wang, Y. Shao, P. Liu, M. S. Whittingham, Next Energy 1 (2023) 100015.

[4] X. Cao, H. Li, Y. Qiao, P. He, Y. Qian, X. Yue, M. Jia, J. Cabana, H. Zhou, Joule 6 (2022) 1290-1303.

[5] X. Zhao, Y. Tian, Z. Lun, Z. Cai, T. Chen, B. Ouyang, G. Ceder, Joule 6 (2022) 1654-1671.

[6] B. Qiu, Y. Qiao, B. Li, Z. Liu, Next Mater. 1 (2023) 100034.

[7] J. Xie, Y. C. Lu, Nat. Commun. 11 (2020) 2499.

[8] J. Sun, H. Yuan, J. Yang, Y.-W. Zhang, J. Wang, Next Mater. 1 (2023) 100024.
[9] S. Scott, Z. Islam, J. Allen, T. Yingnakorn, A. Alflakian, J. Hathaway, A. Rastegarpanah, G. D. J. Harper, E. Kendrick, P. A. Anderson, J. Edge, L. Lander, A. P. Abbott, Next Energy 1 (2023) 100023.
[10] N. Yabuuchi, K. Kubota, M. Dahbi, S. Komaba, Chem. Rev. 114 (2014) 11636-11682.
[11] Z. Cheng, X. Y. Fan, L. Yu, W. Hua, Y. J. Guo, Y. H. Feng, F. D. Ji, M. Liu, Y. X. Yin, X. Han, Y. G. Guo, P. F. Wang, Angew Chem. Int. Edit. 61 (2022) e202117728.
[12] C. Zhao, Q. Wang, ZhenpengYao, J. Wang, B. Sánchez-Lengeling, F. Ding, X. Qi, Y. Lu, X. Bai, BaohuaLi, HongLi, A. Aspuru-Guzik, X. Huang, C. Delmas, M. Wagemaker, L. Chen, Y.-S. Hu, Science 370 (2020) 708–711.
[13] X. Rong, E. Hu, Y. Lu, F. Meng, C. Zhao, X. Wang, Q. Zhang, X. Yu, L. Gu, Y.-S. Hu, H. Li, X. Huang, X.-Q. Yang, C. Delmas, L. Chen, Joule 3 (2019) 503-517.
[14] E. Gabriel, C. Ma, K. Graff, A. Conrado, D. Hou, H. Xiong, eScience (2023).
[15] H. Ren, Y. Li, Q. Ni, Y. Bai, H. Zhao, C. Wu, Adv. Mater. 34 (2022) e2106171.
[16] Y. Xie, M. Saubanère, M. L. Doublet, Energ. Environ. Sci. 10 (2017) 266-274.
[17] Y. Kim, K. H. Ha, S. M. Oh, K. T. Lee, Chemistry 20 (2014) 11980-11992.
[18] Q. Wang, S. Mariyappan, G. Rousse, A. V. Morozov, B. Porcheron, R. Dedryvere, J. Wu, W. Yang, L. Zhang, M. Chakir, M. Avdeev, M. Deschamps, Y. S. Yu, J. Cabana, M. L. Doublet, A. M. Abakumov, J. M. Tarascon, Nat. Mater. 20 (2021) 353-361.
[19] T. Wang, T. Q. Huang, X. L. Li, L. Ma, Y. K. Wang, Y. Qiao, S. P. Gao, Z. Shadike, Z. W. Fu, Angew Chem. Int. Edit. 61 (2022) e202205444.
[20] N. Yabuuchi, K. Yoshii, S. T. Myung, I. Nakai, S. Komaba, J. Am. Chem. Soc. 133 (2011) 4404-4419.
[21] K. Luo, M. R. Roberts, N. Guerrini, N. Tapia-Ruiz, R. Hao, F. Massel, D. M. Pickup, S. Ramos, Y. S. Liu, J. Guo, A. V. Chadwick, L. C. Duda, P. G. Bruce, J. Am. Chem. Soc. 138 (2016) 11211-11218.
[22] E. McCalla, A. M. Abakumov, M. Saubanère, D. Foix, E. J. Berg, G. Rousse, M.-L. Doublet, D. Gonbeau, P. Novák, Gustaaf Van Tendeloo, R. Dominko, J.-M. Tarascon, Science 350 (2015) 1516-1521.
[23] K. Luo, M. R. Roberts, R. Hao, N. Guerrini, D. M. Pickup, Y. S. Liu, K. Edstrom, J. Guo, A. V. Chadwick, L. C. Duda, P. G. Bruce, Nat. Chem. 8 (2016) 684-691.
[24] M. Sathiya, K. Ramesha, G. Rousse, D. Foix, D. Gonbeau, A. S. Prakash, M. L. Doublet, K. Hemalatha, J. M. Tarascon, Chem. Mater. 25 (2013) 1121-1131.
[25] A. J. Perez, D. Batuk, M. Saubanère, G. Rousse, D. Foix, E. McCalla, E. J. Berg, R. Dugas, K. H. W. van den Bos, M.-L. Doublet, D. Gonbeau, A. M. Abakumov, G. Van Tendeloo, J.-M. Tarascon, Chem. Mater. 28 (2016) 8278-8288.
[26] N. Guerrini, L. Jin, J. G. Lozano, K. Luo, A. Sobkowiak, K. Tsuruta, F. Massel, L.-C. Duda, M. R. Roberts, P. G. Bruce, Chem. Mater. 32 (2020) 3733-3740.
[27] K. Wang, Z. Zhang, S. Cheng, X. Han, J. Fu, M. Sui, P. Yan, eScience 2 (2022) 529-536.
[28] R. A. House, H. Y. Playford, R. I. Smith, J. Holter, I. Griffiths, K.-J. Zhou, P. G. Bruce, Energ. Environ. Sci. 15 (2022) 376-383.
[29] R. A. House, J.-J. Marie, M. A. Pérez-Osorio, G. J. Rees, E. Boivin, P. G. Bruce, Nat. Energy 6 (2021) 781-789.
[30] N. Tapia-Ruiz, C. Soares, J. W. Somerville, R. A. House, J. Billaud, M. R. Roberts, P. G. Bruce, J. Power Sources 506 (2021) 230104.

[31] E. Boivin, N. Guerrini, R. A. House, J. G. Lozano, L. Jin, G. J. Rees, J. W. Somerville, C. Kuss, M. R. Roberts, P. G. Bruce, Adv. Funct. Mater. 31 (2020) 2003660.
[32] M. Tamaru, X. Wang, M. Okubo, A. Yamada, Electrochem. Commun. 33 (2013) 23-26.
[33] B. Mortemard de Boisse, G. Liu, J. Ma, S. I. Nishimura, S. C. Chung, H. Kiuchi, Y. Harada, J. Kikkawa, Y. Kobayashi, M. Okubo, A. Yamada, Nat Commun 7 (2016) 11397.
[34] N. Yabuuchi, R. Hara, M. Kajiyama, K. Kubota, T. Ishigaki, A. Hoshikawa, S. Komaba, Adv. Energy Mater. 4 (2014) 1301453.
[35] D. H. Seo, J. Lee, A. Urban, R. Malik, S. Kang, G. Ceder, Nat Chem 8 (2016) 692-697.
[36] N. Yabuuchi, R. Hara, K. Kubota, J. Paulsen, S. Kumakura, S. Komaba, J. Mater. Chem. A 2 (2014) 16851-16855.
[37] U. Maitra, R. A. House, J. W. Somerville, N. Tapia-Ruiz, J. G. Lozano, N. Guerrini, R. Hao, K. Luo, L. Jin, M. A. Perez-Osorio, F. Massel, D. M. Pickup, S. Ramos, X. Lu, D. E. McNally, A. V. Chadwick, F. Giustino, T. Schmitt, L. C. Duda, M. R. Roberts, P. G. Bruce, Nat Chem 10 (2018) 288-295.
[38] G. Assat, J.-M. Tarascon, Nature Energy 3 (2018) 373-386.
[39] J. Zaanen, G. A. Sawatzky, J. W. Allen, Phys Rev Lett 55 (1985) 418-421.
[40] K. Kawai, X.-M. Shi, N. Takenaka, J. Jang, B. M. de Boisse, A. Tsuchimoto, D. Asakura, J. Kikkawa, M. Nakayama, M. Okubo, A. Yamada, Energ. Environ. Sci. 15 (2022) 2591-2600.
[41] X. Rong, J. Liu, E. Hu, Y. Liu, Y. Wang, J. Wu, X. Yu, K. Page, Y.-S. Hu, W. Yang, H. Li, X.-Q. Yang, L. Chen, X. Huang, Joule 2 (2018) 125-140.
[42] E. Boivin, R. A. House, M. A. Pérez-Osorio, J.-J. Marie, U. Maitra, G. J. Rees, P. G. Bruce, Joule 5 (2021) 1267-1280.
[43] P. M. Radjenovic, L. J. Hardwick, Phys. Chem. Chem. Phys. 21 (2019) 1552-1563.
[44] D. Eum, B. Kim, J. H. Song, H. Park, H. Y. Jang, S. J. Kim, S. P. Cho, M. H. Lee, J. H. Heo, J. Park, Y. Ko, S. K. Park, J. Kim, K. Oh, D. H. Kim, S. J. Kang, K. Kang, Nat Mater 21 (2022) 664-672.
[45] K. Dai, J. Wu, Z. Zhuo, Q. Li, S. Sallis, J. Mao, G. Ai, C. Sun, Z. Li, W. E. Gent, W. C. Chueh, Y.-d. Chuang, R. Zeng, Z.-x. Shen, F. Pan, S. Yan, L. F. J. Piper, Z. Hussain, G. Liu, W. Yang, Joule 3 (2019) 518-541.
[46] R. A. House, U. Maitra, L. Jin, J. G. Lozano, J. W. Somerville, N. H. Rees, A. J. Naylor, L. C. Duda, F. Massel, A. V. Chadwick, S. Ramos, D. M. Pickup, D. E. McNally, X. Lu, T. Schmitt, M. R. Roberts, P. G. Bruce, Chem. Mater. 31 (2019) 3293-3300.
[47] G. Assat, S. L. Glazier, C. Delacourt, J.-M. Tarascon, Nat. Energy 4 (2019) 647-656.
[48] K. Zhang, D. Kim, Z. Hu, M. Park, G. Noh, Y. Yang, J. Zhang, V. W. Lau, S. L. Chou, M. Cho, S. Y. Choi, Y. M. Kang, Nat. Commun. 10 (2019) 5203.
[49] X. Bai, M. Sathiya, B. Mendoza-Sánchez, A. Iadecola, J. Vergnet, R. Dedryvère, M. Saubanère, A. M. Abakumov, P. Rozier, J.-M. Tarascon, Adv. Energy Mater. 8 (2018) 1802379.
[50] A. Gao, Q. Zhang, X. Li, T. Shang, Z. Tang, X. Lu, Y. Luo, J. Ding, W. H. Kan, H. Chen, W. Yin, X. Wang, D. Xiao, D. Su, H. Li, X. Rong, X. Yu, Q. Yu, F. Meng, C. Nan, C. Delmas, L. Chen, Y.-S. Hu, L. Gu, Nature Sustainability 5 (2021) 214-224.
[51] B. Kim, J.-H. Song, D. Eum, S. Yu, K. Oh, M. H. Lee, H.-Y. Jang, K. Kang, Nat. Sustain. 5 (2022) 708-716.
[52] P. Wang, H. Yao, Xinyu Liu, Y. Yin, J. Zhang, Y. Wen, X. Yu, L. Gu, Y. Guo, Sci. Adv. 4 (2018) eaar6018.
[53] C. Masquelier, M. Tabuchi, K. Ado, R. Kanno, Y. Kobayashi, Y. Maki, O. Nakamura, J. B.

Goodenough, J. Solid State Chem. 123 (1996) 255–266.
[54] Z. Lu, J. R. Dahn, J. Electrochem. Soc. 148 (2001) A1225-A1229.
[55] S. Kumakura, Y. Tahara, K. Kubota, K. Chihara, S. Komaba, Angew Chem. Int. Edit. 55 (2016) 12760-12763.
[56] N. Yabuuchi, M. Kajiyama, J. Iwatate, H. Nishikawa, S. Hitomi, R. Okuyama, R. Usui, Y. Yamada, S. Komaba, Nat. Mater. 11 (2012) 512-517.
[57] R. J. Clément, J. Billaud, A. Robert Armstrong, G. Singh, T. Rojo, P. G. Bruce, C. P. Grey, Energ. Environ. Sci. 9 (2016) 3240-3251.
[58] K. Xu, Chem. Rev. 104 (2004) 4303−4417.
[59] S. Wu, B. Su, K. Ni, F. Pan, C. Wang, K. Zhang, D. Y. W. Yu, Y. Zhu, W. Zhang, Adv. Energy Mater. 11 (2020) 2002737.
[60] P. K. Nayak, E. M. Erickson, F. Schipper, T. R. Penki, N. Munichandraiah, P. Adelhelm, H. Sclar, F. Amalraj, B. Markovsky, D. Aurbach, Adv. Energy Mater. 8 (2018) 1702397.
[61] C. Zhao, C. Li, H. Liu, Q. Qiu, F. Geng, M. Shen, W. Tong, J. Li, B. Hu, J. Am. Chem. Soc. 143 (2021) 18652-18664.
[62] R. A. House, U. Maitra, M. A. Perez-Osorio, J. G. Lozano, L. Jin, J. W. Somerville, L. C. Duda, A. Nag, A. Walters, K. J. Zhou, M. R. Roberts, P. G. Bruce, Nature 577 (2020) 502-508.
[63] B. Mortemard de Boisse, S.-i. Nishimura, E. Watanabe, L. Lander, A. Tsuchimoto, J. Kikkawa, E. Kobayashi, D. Asakura, M. Okubo, A. Yamada, Adv. Energy Mater. 8 (2018) 1800409.
[64] J. Liu, R. Qi, C. Zuo, C. Lin, W. Zhao, N. Yang, J. Li, J. Lu, X. Chen, J. Qiu, M. Chu, M. Zhang, C. Dong, Y. Xiao, H. Chen, F. Pan, Nano Energy 88 (2021) 106252.
[65] Q. Wang, Y. Liao, X. Jin, C. Cheng, S. Chu, C. Sheng, L. Zhang, B. Hu, S. Guo, H. Zhou, Angew Chem. Int. Edit. 61 (2022) e202206625.
[66] X. L. Li, J. Bao, Z. Shadike, Q. C. Wang, X. Q. Yang, Y. N. Zhou, D. Sun, F. Fang, Angew Chem. Int. Edit. 60 (2021) 22026-22034.
[67] X. L. Li, T. Wang, Y. Yuan, X. Y. Yue, Q. C. Wang, J. Y. Wang, J. Zhong, R. Q. Lin, Y. Yao, X. J. Wu, X. Q. Yu, Z. W. Fu, Y. Y. Xia, X. Q. Yang, T. Liu, K. Amine, Z. Shadike, Y. N. Zhou, J. Lu, Adv. Mater. 33 (2021) e2008194.
[68] Q. Shen, Y. Liu, X. Zhao, J. Jin, X. Song, Y. Wang, X. Qu, L. Jiao, Adv. Energy Mater. 13 (2022) 2203216.
[69] C. Vaalma, D. Buchholz, S. Passerini, J. Power Sources 364 (2017) 33-40.
[70] Y. J. Guo, P. F. Wang, Y. B. Niu, X. D. Zhang, Q. Li, X. Yu, M. Fan, W. P. Chen, Y. Yu, X. Liu, Q. Meng, S. Xin, Y. X. Yin, Y. G. Guo, Nat. Commun. 12 (2021) 5267.
[71] Q. C. Wang, J. K. Meng, X. Y. Yue, Q. Q. Qiu, Y. Song, X. J. Wu, Z. W. Fu, Y. Y. Xia, Z. Shadike, J. Wu, X. Q. Yang, Y. N. Zhou, J Am Chem Soc 141 (2019) 840-848.
[72] Y. Huang, Y. Zhu, A. Nie, H. Fu, Z. Hu, X. Sun, S. C. Haw, J. M. Chen, T. S. Chan, S. Yu, G. Sun, G. Jiang, J. Han, W. Luo, Y. Huang, Adv Mater 34 (2022) e2105404.
[73] C. Zhao, Z. Yao, J. Wang, Y. Lu, X. Bai, A. Aspuru-Guzik, L. Chen, Y.-S. Hu, Chem 5 (2019) 2913-2925.
[74] Y. Wang, X. Zhao, J. Jin, Q. Shen, Y. Hu, X. Song, H. Li, X. Qu, L. Jiao, Y. Liu, J. Am. Chem. Soc. 145 (2023) 22708-22719.
[75] C. Wang, L. Liu, S. Zhao, Y. Liu, Y. Yang, H. Yu, S. Lee, G. H. Lee, Y. M. Kang, R. Liu, F. Li, J. Chen, Nat. Commun. 12 (2021) 2256.
[76] Y. Wang, X. Zhao, J. Jin, Q. Shen, N. Zhang, X. Qu, Y. Liu, L. Jiao, Energy Storage Mater. 47 (2022)

44-50.
[77] J. Jin, Y. Liu, Q. Shen, X. Zhao, J. Zhang, Y. Song, T. Li, X. Xing, J. Chen, Adv. Funct. Mater. 32 (2022) 2203424.
[78] Y. Jin, Y. Xu, B. Xiao, M. H. Engelhard, R. Yi, T. D. Vo, B. E. Matthews, X. Li, C. Wang, P. M. L. Le, J. G. Zhang, Adv. Funct. Mater. 32 (2022).
[79] W. Zuo, X. Liu, J. Qiu, D. Zhang, Z. Xiao, J. Xie, F. Ren, J. Wang, Y. Li, G. F. Ortiz, W. Wen, S. Wu, M. S. Wang, R. Fu, Y. Yang, Nat. Commun. 12 (2021) 4903.
[80] K. Tang, Y. Huang, X. Xie, S. Cao, L. Liu, M. Liu, Y. Huang, B. Chang, Z. Luo, X. Wang, Chem. Eng. J. 384 (2020) 123234.
[81] Q. Li, Y. Qiao, S. Guo, K. Jiang, Q. Li, J. Wu, H. Zhou, Joule 2 (2018) 1134-1145.
[82] S. Yang, W. Ren, J. Chen, Front. Energy 11 (2017) 374-382.
[83] T. Wang, G. X. Ren, Z. Shadike, J. L. Yue, M. H. Cao, J. N. Zhang, M. W. Chen, X. Q. Yang, S. M. Bak, P. Northrup, P. Liu, X. S. Liu, Z. W. Fu, Nat. Commun. 10 (2019) 4458.
[84] J. Vergnet, M. Saubanère, M.-L. Doublet, J.-M. Tarascon, Joule 4 (2020) 420-434.
[85] S. F. Linnell, E. J. Kim, Y.-S. Choi, M. Hirsbrunner, S. Imada, A. Pramanik, A. F. Cuesta, D. N. Miller, E. Fusco, B. E. Bode, J. T. S. Irvine, L. C. Duda, D. O. Scanlon, A. R. Armstrong, Journal of Materials Chemistry A 10 (2022) 9941-9953.
[86] Q. Shen, Y. Liu, L. Jiao, X. Qu, J. Chen, Energy Storage Mater. 35 (2021) 400-430.
[87] Y. Liu, J. Li, Q. Shen, J. Zhang, P. He, X. Qu, Y. Liu, eScience 2 (2022) 10-31.
[88] K. Xu, Chem. Rev. 114 (2014) 11503-11618.